Cardiovascular Engineering and Technology, Vol. 10, No. 4, December 2019 *(© 2019)* pp. 590–603
https://doi.org/10.1007/s13239-019-00425-2

Original Article

Automated Detection of Vulnerable Plaque for Intravascular Optical Coherence Tomography Images

Ran Liu,[1,2] Yanzhen Zhang,[1] Yangting Zheng,[2] Yaqiong Liu,[2] Yang Zhao,[2] and Lin Yi[3]

[1]School of Microelectronics and Communication Engineering, Chongqing University, Chongqing 400044, China; [2]College of Computer Science, Chongqing University, Chongqing 400044, China; and [3]Chongqing University Cancer Hospital/Chongqing Cancer Institute/Chongqing Cancer Hospital, Chongqing 400030, China

(Received 16 November 2018; accepted 4 July 2019; published online 18 September 2019)

Associate Editors Ajit P. Yoganathan and Zhongjun Wu oversaw the review of this article.

Abstract
Purpose—Vulnerable plaque detection is important to acute coronary syndrome (ACS) diagnosis. In recent years, intravascular optical coherence tomography (IVOCT) imaging has been used for vulnerable plaque detection. Current automated detection methods adopt the traditional image classification and object detection algorithms, such as the logistic regression model, SVM, and Haar-Adaboost, to detect vulnerable plaques. The detection quality of these methods is relatively low. The aim of this study is to improve the detection quality of vulnerable plaque.
Methods—We propose an automatic detection system of vulnerable plaque for IVOCT images based on deep convolutional neural network (DCNN). The system is mainly composed of four modules: pre-processing, deep convolutional neural networks (DCNNs), post-processing, and ensemble. The IVOCT images input to DCNNs are firstly pre-processed by using the methods of de-noising and data augmentation. Then multiple DCNNs are used to detect the vulnerable plaques in the IVOCT images; the vulnerable plaque regions and their corresponding labels and scores are output. Next, the output results of each network are processed by the post-processing module. We propose three algorithms, union of intersecting regions, duplicated region processing, and small gaps removal for post-processing. Finally, the output detection results of multiple networks are combined using a proposed combining method in ensemble module.
Results—We evaluated the proposed method in a dataset of 300 IVOCT images. Experimental results show that our system can achieve a precision rate of 88.84%, a recall rate of 95.02%, and an overlap rate of 85.09%; the detection quality score is 88.46%.
Conclusions—The proposed algorithms can detect vulnerable plaques with superior performance; our system can be used as an auxiliary diagnostic tool for vulnerable plaque detection in IVOCT images.

Address correspondence to Lin Yi, Chongqing University Cancer Hospital/Chongqing Cancer Institute/Chongqing Cancer Hospital, Chongqing 400030, China. Electronic mail: lin_yi@cqprecision.cn

Keywords—Intravascular optical coherence tomography (IVOCT), Acute coronary syndrome (ACS), Vulnerable plaque, Convolutional neural network, Plaque detection.

ABBREVIATIONS

ACS	Acute coronary syndrome
AUC	Area under the curve
CAD	Coronary artery disease
DSC	Dice similarity coefficient
DCNN	Deep convolutional neural network
Faster R-CNN	Faster region-convolutional neural network
IVOCT	Intravascular optical coherence tomography
IVUS	Intravascular ultrasound
mAP	Mean average precision
pp	Percentage point
RPN	Region proposal network
ROC	Receiver operating characteristic
SSD	Single shot multibox detector
TCFA	Thin-cap fibroatheroma
YOLO	You only look once

INTRODUCTION

Coronary artery disease (CAD) is the most common cause of death in the world.[26] Among them, *acute coronary syndrome* (ACS) is the most dangerous condition. Several serial angiographic studies have demonstrated that nearly 70% of ACS events are

caused by the *vulnerable plaque rupture* of *coronary atherosclerosis*.[21] Therefore, the vulnerable plaque of coronary atherosclerosis is the main cause of ACS, and clinical risk prediction of vulnerable plaque is important for early intervention and treatment.[9]

Vulnerable plaques are usually characterized by large *lipid cores*, thin *fibrous caps*, and *macrophage infiltration*.[4,5,21,24] Detection of vulnerable plaque depends on *intravascular imaging modality*.[5,12] At present, *intravascular ultrasound* (IVUS) imaging and *intravascular optical coherence tomography* (IVOCT) imaging are the two commonly used intracoronary imaging modalities.[2,14] The greatest advantage of IVOCT is its high resolution (10–20 μm), which is about 10 times higher than that of IVUS.[5,26] Previous studies show that IVOCT has better sensitivity and specificity for the detection of vulnerable plaques when compared to IVUS.[11,13] In addition, this non-occlusive technique of IVOCT image acquisition is safe and useful and promises to shorten the procedure.[12] Thus, IVOCT technology is more suitable for the detection of vulnerable plaque.

Traditionally, cardiologists diagnose whether there are vulnerable plaques on IVOCT images according to their experience. Such a manual method is time-consuming and subjective.[7,29] In order to overcome these disadvantages, it is necessary to develop an automatic detection method for vulnerable plaque in coronary atherosclerosis. In the previous study, Wang et al. proposed a computer-aided method that allows volumetric analysis of fibrous cap to analyze vulnerable plaque.[26] Since then, they have proposed a *logistic regression model* to significantly simplify the diagnosis of vulnerable plaques.[27] Xu et al. presented an automatic atherosclerotic disease detection system on IVOCT images. The system first preprocesses the IVOCT images and then a linear *support vector machine* (SVM) classifier is employed to detect the unhealthy subject.[29] Based on this system, they increased the image data and improved the preprocessing method and the SVM classifier to make the classification finer and more accurate.[30]

The studies above adopt the traditional *image classification* and *object detection* methods for vulnerable plaque detection. Image classification analyzes the numerical properties of various image features and organizes data into categories.[19,23] This task requires marking the image based on the contents of the image and then predicting the most suitable label by the designed classifier.[30] Object detection is more complicated than image classification where one must localize and identify the *objects of interest* in an image.[3] Object detection is a challenging task due to the large changes in size, attitude, position, and the number of objects.[17] Traditional object detection algorithms include Haar-Adaboost,[25] HOG-SVM[3] and so on. In recent years, many *deep convolutional neural network* (DCNN), such as YOLO,[18] SSD,[16] and Faster R-CNN,[20] have demonstrated excellent performance in medical image analysis, and have been widely used in the task of recognition, detection and segmentation of lesion with large labeled dataset. However, for IVOCT technique, it is usually difficult to get large labeled training dataset. In addition, the imaging principle of IVOCT is quite different from that of natural scene images or other medical images. Therefore, it is necessary to propose new algorithms to improve the detection performance according to the characteristics of the IVOCT.[3]

This paper presents an automatic system for vulnerable plaque detection in IVOCT images. As shown in Fig. 1, the system consists of four modules: pre-processing, DCNN, post-processing, and ensemble. The pre-processing module boosts the performance of each deep convolutional neural network by *de-noising* and *data augmentation*. The DCNN module consists of multiple networks; it performs the detection function of the vulnerable plaque after being trained. The post-processing module processes the *vulnerable plaque regions* output by the DCNN module during the *testing stage*. The ensemble module combines the output results from post-processing module according to a proposed ensemble method; hence, the generalized performance of the system can be significantly improved and the better *detection quality* can be achieved.[15]

Note that DCNN is commonly used for object detection for natural scene images or other medical image analysis. For the IVOCT images, we need special pre-processing and post-processing method for DCNN. In addition, multiple DCNNs should be used to form an ensemble and the output of these networks should be combined to obtain better performance. Therefore, this paper focuses on the pre-processing, post-processing and ensemble methods.

MATERIALS AND METHODS

IVOCT Image

This work was performed with approval by the Institutional Review Board (IRB) of Chongqing University Cancer Hospital (ERN050, July 5th, 2018). IVOCT image obtained from the patient consists of the bright *vessel tissue region* and the dark *lumen region*.[28] Vulnerable plaques (i.e. thin-cap fibroatheroma [TCFA][30]) appear in the bright vessel tissue region.[28] Vulnerable plaque is characterized as a plaque containing a large lipid necrotic core covered by a thin fibrous cap (< 65 μm) infiltrated by macrophages.[12,26]

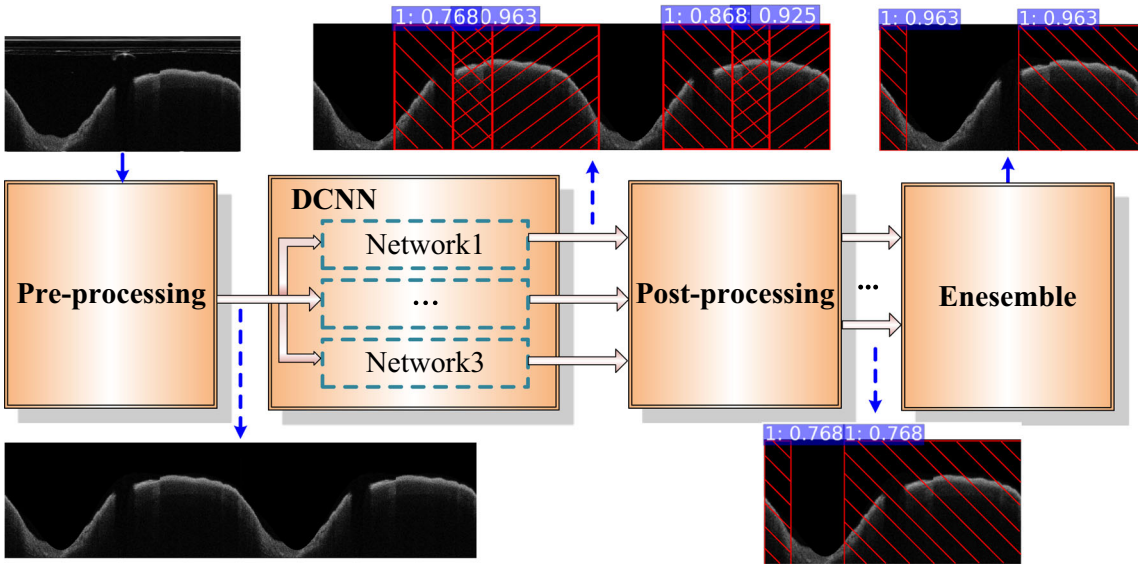

FIGURE 1. Flowchart of the proposed system. The system consists of four modules.

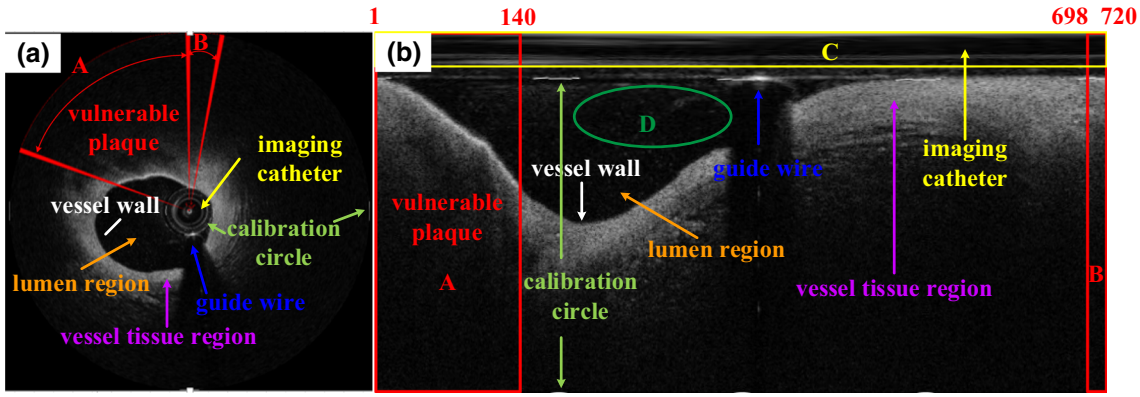

FIGURE 2. An IVOCT image with vulnerable plaques. (a) an IVOCT image in the Cartesian coordinate system. The vulnerable plaque, guide wire, imaging catheter, vessel wall, vessel tissue region, and lumen region are marked with different colors. The guide wire has a high reflection followed by a long dark shadow. (b) The converted IVOCT image in the polar coordinate system, resolution: 720 × 352 (width × height).

The dataset used in this paper consist of 2000 training images and 300 test images. The training images consist of 1000 positive samples containing vulnerable plaque and 1000 negative samples without vulnerable plaque; the test images contain 198 positive and 102 negative samples. Vulnerable plaques in IVOCT image were manually labeled by medical experts. Figure 2a shows a positive sample. It is a single-channel 8-bit grayscale image. In order to facilitate the algorithm design, Fig. 2a is transformed from the *Cartesian coordinate system* to the *polar coordinate system*, as shown in Fig. 2b. Figure 2b is also an 8-bit grey-scale image.

Note the vulnerable plaque regions manually marked by the cardiologists is only represented by column indexes of pixels. As shown in Fig. 2b, vulnerable plaque region A can be expressed as an *ordered pair* $\langle 1, 140 \rangle$, and vulnerable plaque region B can be expressed as an ordered pair $\langle 698, 720 \rangle$. As this image is a positive sample, we label it with "1". A negative sample will be labeled with "0". In this paper, the vulnerable plaque regions are rectangular and the height of the rectangular is equal to the height of the image. However, it should be emphasized that the regions manually marked by the cardiologists contain vulnerable plaque, and not the entire region is a vulnerable plaque. Vulnerable plaques appear in the bright vessel tissue region. The dark lumen region does not contain any information related to vulnerable plaque.

Vulnerable Plaque Detection Algorithm

In this section, we propose an automatic detection system for vulnerable plaque. The input of the system is 720 × 352 IVOCT images. In the training stage, the

system outputs a trained model; in the testing stage, the system outputs the detection result of the vulnerable plaque. The details of each module in the system are addressed in the following sections.

Pre-processing

It can be seen from Fig. 2b that there is significant noise in the image, such as *imaging catheter* (in region C), *calibration circle,* and the noise above the vessel wall (e.g., noise in region D). This noise will greatly reduce the performance of the DCNN when detecting vulnerable plaques. Therefore, it is necessary to de-noise the image input to the DCNN module. In addition, the training of networks requires a large training dataset, but there are only 2000 training images in our study, which is too small to meet the needs of training. In this study, we adopted the method of *data augmentation* to increase the training samples.

Pre-processing module is designed to perform two functions: de-noising and data augmentation.

De-noising

All the bright components inside the lumen should be removed before the intracavitary contour detection. Firstly, we need to remove the imaging catheter from the IVOCT image. As shown in Fig. 2b, the imaging catheter is located above the calibration circle and its shape is linear. There are overlaps between the vessel wall and the imaging catheter in some images. To avoid losing this portion of the vessel wall, we removed only a portion of the imaging catheter. For example, we assign all the pixel values in the region C to zero (Fig. 3a).

Secondly, we need to remove the calibration circle of the IVOCT image. As shown in Fig. 2b, the calibration circle appears at the top and bottom of the image. The calibration circle at the top negatively affects the subsequent intracavitary counter detection, making the intracavitary counter detection inaccurate, so the calibration circle must be removed first. We assign all pixel values of the calibration circle to zero and the result is shown in Fig. 3b. Compared with Fig. 3a, the originally highlighted calibration circle in the green rectangle has been removed. It should be noted that the position of the calibration circle in each image is the same. We need only to assign all pixel values in the same position to zero, and then all the calibration circles are removed.

Finally, we need to remove the intracavitary noise above the vessel wall from the IVOCT image. Two steps are involved. We take Fig. 3b as an example to illustrate the method:

Step 1: *Intracavitary contour* detection. In this step, Fig. 3b is converted to a binary image firstly, then it is processed by *mathematical morphological operation*: *dilation* first and then *erosion*.[8] After that, we connect the highest point of each column of white pixels to get rough intracavitary contours of the vessel wall, which is shown as the blue curve in Fig. 3c. Because the blue curve is too rough, next we use a *high-order*

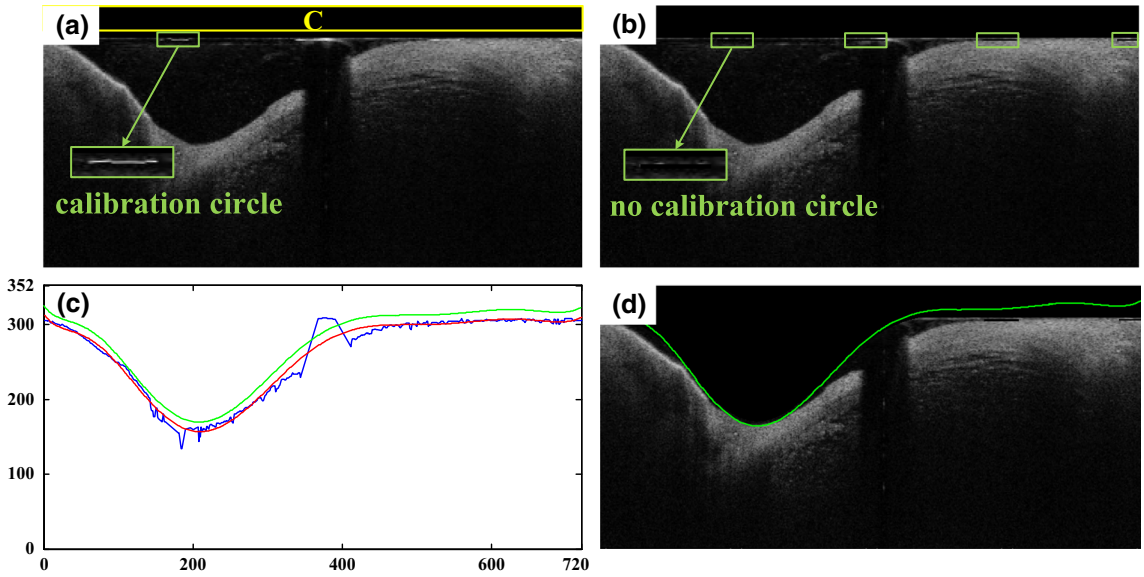

FIGURE 3. Pre-processing results of IVOCT image, taking Fig. 2b as an example. (a) Imaging catheter is removed. (b) Calibration circle is removed. (c) *Intracavitary contour* detection of the vessel wall in b. (d) *The intracavitary noise* above the vessel wall is removed.

function to fit the blue curve and get the red curve (shown in Fig. 3c). In order to prevent the loss of information of the vessel wall, we move the red curve up a certain distance and get the green curve. We use the green curve as the intracavitary contour of the vessel wall

Step 2: Intracavitary noise removal. In order to remove intracavitary noise, we assign the pixel values above the green curve to zero. Figure 3d shows the image after removing the intracavitary noise above the vessel wall

Data Augmentation

Data augmentation refers to the process of creating new similar samples to the training set and can be seen as one kind of regularization technology. Selection of appropriate data augmentation strategies is very important. Therefore, in order to have a good effect, it is necessary to analyze the location of vulnerable plaque in IVOCT images.

In the positive sample, some vulnerable plaques are located on the left and right edges of the image, for instance, the vulnerable plaque regions A and B in Fig. 4a. In fact, in the Cartesian coordinate system, the vulnerable plaque regions A and B are adjacent (in Fig. 2a). In order to keep their topological relationship unchanged, we connect Fig. 4a end-to-end to form an image of resolution 1440 × 352, as shown in Fig. 4b. We call the region ⟨1, 720⟩ *original region* Ω; the region ⟨721, 1440⟩ *duplicated region* Ω′. By this way, vulnerable plaques on the left and right edges are connected together and merged into a new vulnerable plaque region located in the middle of the new image (region C in Fig. 4b), new samples are created. It can help to increase the number of images. In addition, the right topological relationship can be learned by DCNNs.

All the positive and negative samples are subjected to end-to-end connection, and 10 IVOCT images of resolution of 720 × 352 are extracted at an equal interval (40 pixels) from each IVOCT image of resolution 1440 × 352. The starting *horizontal coordinate* (column index) of the first image is 260 in the connected image. By this way, we can make the 10 images that contain the *end-to-end connected region* (e.g., region C in Fig. 4b) as much as possible. The relative location of the same plaque in each extracted image is different. During the training stage, DCNN treats them as different samples.

Next, we flip the augmented 10 × 2000 IVOCT images in the horizontal direction.[23] Hence, the number of images increases 20 times compared with the original. Flipping might change the relative location of a plaque in IVOCT image, it can help to increase the number of sample image for DCNN training. Finally, each image is connected end-to-end to itself to obtain 40,000 images of resolution 1440 × 352.

Please note that when the images are preprocessed, the corresponding *column index ordered pair* of the vulnerable plaque regions should also be processed. For example, the vulnerable plaque regions A and B in Fig. 4a become the vulnerable plaque regions A, B, A′, and B′ in Fig. 4b after an end-to-end connection. Obviously, B and A′ should be combined into a larger region C. The corresponding column index ordered pair should also be combined into column index ordered pair of region C accordingly.

DCNN

Our DCNN module consists of multiple networks. They are all DCNNs. The same type of network is used here because other results have shown that using one type of learning network for constructing ensembles is more convenient and effective and easier to organize.[15] We selected proper DCNNs for ensembling from a group of candidate networks.[15] There are three candidate networks in this group: YOLO, SSD, and Faster R-CNN.

YOLO is a new approach to object detection, which frames *object detection* as a regression problem to spatially separated bounding boxes and associated class probabilities.[18] This method uses a single neural network to predict bounding boxes and class probabilities directly from full images in one evaluation and achieves end-to-end object detection. We train YOLO from scratch because we want to play with different *training regimes*, *hyper-parameters*, or datasets. We use a small network (tiny-yolo-voc.cfg) for training. Dur-

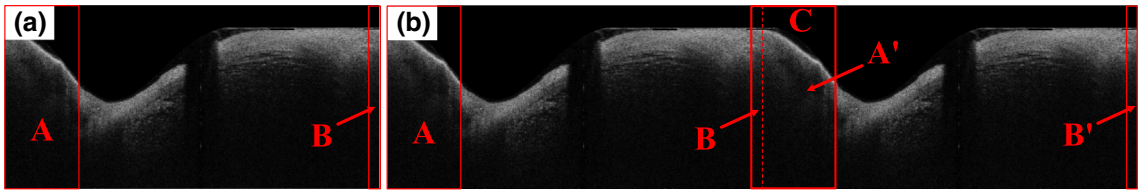

FIGURE 4. Illustration of the end-to-end connection of IVOCT images. (a) De-noised image with vulnerable plaques marked. (b) End-to-end connected image with vulnerable plaques marked.

ing the training stage, the trained weights are saved with the number of iterations.

SSD is a method for detecting objects in images using a single deep neural network.[16] Compared with the YOLO that operated on a single scale *feature map*, they add convolutional feature layers to the end of the truncated base network. These layers decrease in size progressively and allow predictions of detections at multiple scales.

Faster R-CNN shows strong advantages in object detection. It introduces a *region proposal network* (RPN) that shares full-image convolutional features with the *detection network*.[20] An RPN is a fully convolutional network that simultaneously predicts object bounds and *objectness scores* at each position. One important aspect of the RPN is that it can classify and regress bounding boxes of vulnerable plaques with reference to *anchor boxes* of multiple *scales* and *aspect ratios*; as a result, it can generate high-quality *region proposals*.[20] Faster R-CNN can be initialized by pre-training a model for ImageNet classification, as a standard practice.[20] There are three models after pre-training: a small model ZF, a medium model VGG_CNN_M_1024, and a large model VGG-16. Considering the size of our sample, we used the medium model VGG_CNN_M_1024 as a pre-trained model for Faster R-CNN. Then we fine-tune the Faster R-CNN using the labeled IVOCT images.

Please note that the output of the pre-processing module serves as the input of all the networks in DCNN module in the training stage; in the test stage, the output of the networks serves as the input of post-processing module.

Post-processing

Each network in DCNN module might detect multiple vulnerable plaques in an IVOCT image of resolution 1440 × 352; the topological relationships among these regions, or the topological relationships between the regions and image borders may vary. In order to obtain better detection quality, we need to post-process the results obtained by DCNN module. Each step in the post-processing is described in detail below.

Union of Intersecting Regions

First, we detect whether there is an intersecting region in a 1440 × 352 IVOCT image **I**. Assume that the vulnerable plaque regions detected in the image **I** are B_1, B_2,…, B_m, and their corresponding scores are s_1, s_2,…, s_m. If

$$B_i \cap B_j \neq \emptyset,\ 1 \leq i < j \leq m \tag{1}$$

then the union of B_i and B_j can be obtained:

$$\begin{cases} C_k = B_i \cup B_j \\ s_k = \min(s_i, s_j) \end{cases},\ k \in [1, m), \quad 1 \leq i < j \leq m \tag{2}$$

Performing union operations on all the vulnerable plaques in an image according to (1) and (2) allows all the processed vulnerable plaques in this image disjoint to each other.

Duplicated Region Processing

After the union of intersecting regions, we start processing of duplicated region. The purpose of processing the duplicated region is to retrieve undetected object in the original region Ω from duplicated region Ω' to improve the *recall rate*. This processing is subject to two situations:

(1) If the vulnerable plaque region $B_i < x'_1, x'_2 >$ detected in the image **I** meets:

$$(\forall B_i)(B_i \subseteq \mathrm{I} \rightarrow B_i \subseteq \Omega'), \quad 1 \leq i \leq m \tag{3}$$

then it indicates that the vulnerable plaque region only appears in the duplicated region Ω', as shown in Fig. 5a. In this case, we will map B_i into the original region Ω:

$$C_k\langle x_1, x_2\rangle = C_k\langle x'_1 - \text{width},\ x'_2 - \text{width}\rangle,\ k \in [1, m),\ 1 \leq i \leq m \tag{4}$$

where the width in (4) is the width of the image without end-to-end connection. In this paper width = 720. The result after mapping is shown in Fig. 5b.

(2) If the vulnerable plaque region B_i detected in the image **I** meets:

$$((B_i \cap \Omega \neq \Phi) \wedge (B_i \cap \Omega' \neq \Phi)) \tag{5}$$

then it indicates that B_i crosses both the original region Ω and duplicated region Ω', as shown in Fig. 5c. In this case, we will map $B_i \cap \Omega'$ into the original region Ω:

$$C_k\langle x_1, x_2\rangle = (B_i \cap \Omega')\langle(\text{width} + 1) - \text{width}, x'_2 - \text{width}\rangle,\ k \in [1, m),\ 1 \leq i \leq m \tag{6}$$

The result after mapping is shown in Fig. 5d.

After the processing above, only the detection results in the original region are kept.

Small Gaps Removal

There may be a small gap between the bound of the vulnerable plaque region and the left or right edge of the image after duplicated region processing. Here, the small gap is a gap that the width of which is no more than w_g (unit: pixel, w_g = 10 in our experiments).

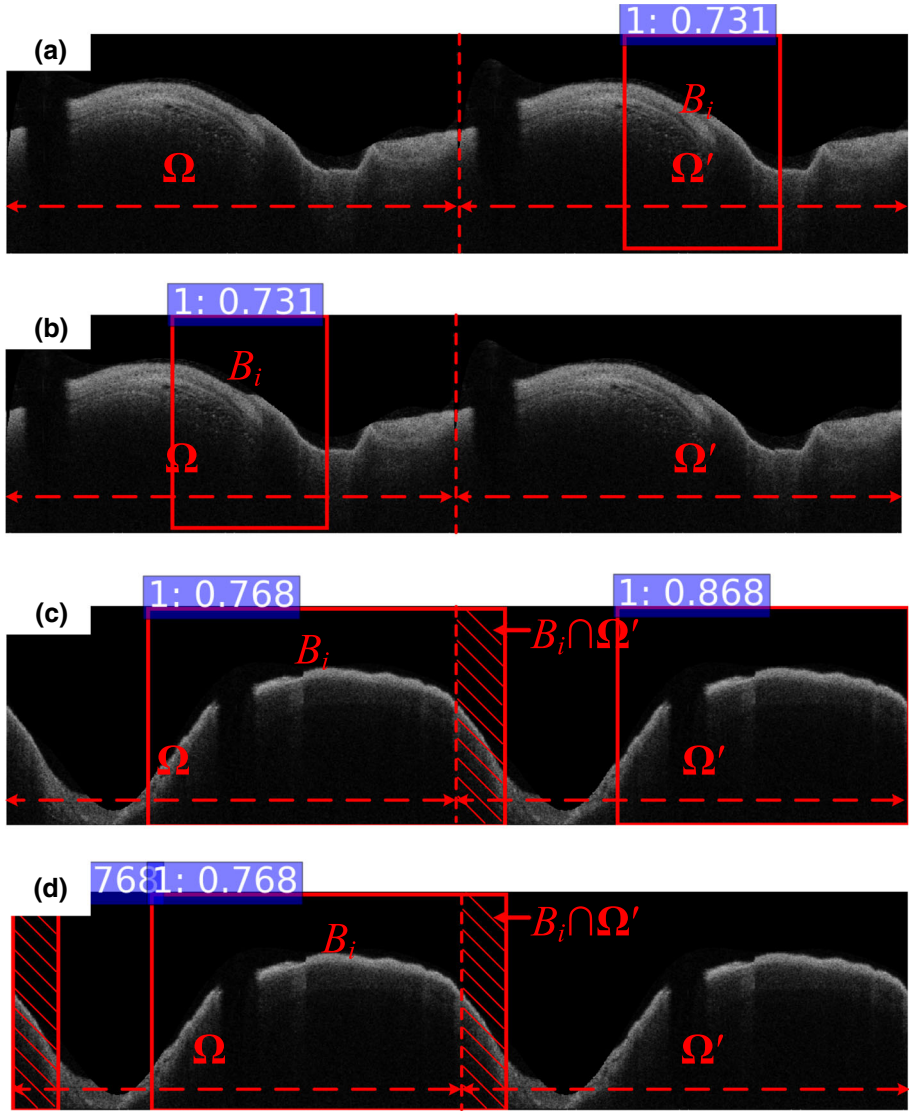

FIGURE 5. Illustration of duplicated region processing. (a) Vulnerable plaque region is detected only in the duplicated region Ω′. (b) The vulnerable plaque region in a is mapped to the original region Ω. (c) There is a vulnerable plaque region B_i across the original region Ω and the duplicated region Ω′. (d) $B_i \cap \Omega'$ in a is mapped to the original region Ω

In an IVOCT image of width × height, the region $G_L < 1, w_g >$ is called *left gap region*, the region $G_R <$ width $- w_g$, width $>$ is called *right gap region*.

If the left most vulnerable plaque region A $< x_{l1}, x_{l2} >$ and the rightmost vulnerable plaque region B $< x_{r1}, x_{r2} >$ meets:

$$(A \cap G_L \neq \Phi) \wedge (B \cap G_R \neq \Phi) \tag{7}$$

then it indicates that A and B are adjacent or very close in the Cartesian coordinate system; A and B may be one vulnerable plaque region. Therefore, it was reasonable to combine A and B into one. Here we extend the region of the vulnerable plaque A and B into A′ and B′ according to (8) to remove the small gaps. Thus, region A and region B are actually merged.

$$\begin{cases} A' < x'_{l1}, x'_{l2} > = A < x_{l1} - x_{l1} + 1, x_{l2} > \\ B' < x'_{r1}, x'_{r2} > = B < x_{r1}, \text{width} > \end{cases} \tag{8}$$

Ensemble

After post-processing, each network outputs its detection results of the same IVOCT image. The results include the label of the image (positive or negative sample), vulnerable plaque regions and their corresponding scores. These results are combined in this module. The ensemble method is described as follows.

Step 1 IVOCT image classification.
In this step, we need to determine whether the image is a positive or negative sample from the labels outputted by DCNNs. Here we add Haar-Adaboost to assist in classification because it shows high performance in classifying negative samples. If a sample is classified as a negative sample by Haar-Adaboost, then it will be eventually labeled as a negative sample with a high probability by our combining method. Table 1 lists the rules for IVOCT image classification.

Step 2: Vulnerable plaque region mergence.
Assume that the vulnerable plaque regions set detected by network i in DCNN module is $R_i = \{\Sigma_{\iota 1}, \Sigma_{\iota 2}, \ldots, \Sigma_{\iota v}\}$, and the vulnerable plaque regions set detected by network j in DCNN module is $R_j = \{\Sigma_{\varphi 1}, \Sigma_{\varphi 2}, , \Sigma_{\varphi \mu}\}$. Set C is the vulnerable plaque regions set output by the ensemble module. If

$$R_{ip} \cap R_{jq} = \emptyset,\ 1 \le p \le n,\ 1 \le q \le m, \quad i \ne j \tag{9}$$

then we calculate the union of R_{ip} and R_{jq} by

$$C = C \cup \left\{R_{ip} \cup R_{jq}\right\},\ 1 \le p \le n,\ 1 \le q \le m, \quad i \ne j \tag{10}$$

else

$$C = \begin{cases} C \cup \left\{R_{ip}\right\} \\ C \cup \left\{R_{jq}\right\} \end{cases},\ 1 \le p \le n,\ 1 \le q \le m, \quad i \ne j \tag{11}$$

TABLE 1. Rules for IVOCT image classification.

Haar-Adaboost	YOLO	SSD	Faster R-CNN	Class
*	0	0	0	0
0	0	0	1	0
0	0	1	0	0
0	0	1	1	0
0	1	0	0	0
0	1	0	1	0
0	1	1	0	0
*	1	1	1	1
1	0	0	1	1
1	0	1	0	1
1	0	1	1	1
1	1	0	0	0
1	1	0	1	1
1	1	1	0	1

"0": negative sample; "1" positive sample. "*" means the class can be either "0" or "1". Class in the last column is the final classification result.

The above combining rule ensures that all the detected vulnerable plaque regions of the networks will be output, and the intersecting regions will be merged before output.

Evaluation Metrics

As can be seen from Fig. 2b, IVOCT images have their own characteristics. Traditional evaluation metrics for object detection, such as *mean average precision* (mAP), cannot evaluate the detection quality of vulnerable plaque detection effectively. For the evaluation of medical image analysis performance, people usually consider metrics such as *Dice Similarity Coefficient* (DSC), *sensitivity* and *specificity*.[1] DSC can be viewed as a similarity measure over sets. In this paper, it is used to measure the *overlap rate* between the detected vulnerable plaque regions and the real vulnerable plaque regions.

Assume the real vulnerable plaque regions set is $A = \{A_1, A_2, \ldots, A_n\}$, and the vulnerable plaque regions set detected by the system is $B = \{B_1, B_2, \ldots, B_m\}$. Note that there might be an intersection between the vulnerable plaque region B_i $(1 \le i \le m)$ and B_j $(1 \le j \le m)$ detected by the system. For this case, we regard B_i and B_j as the wrong output (because there is no intersection between the elements in the set A). These regions should be excluded from the set B by (12) before the evaluation metrics calculation.

$$B_i \cap B_j = \emptyset, i, j \in [1, m], \quad i \ne j \tag{12}$$

The DSC can be calculated by

$$\mathrm{DSC}(A_i, B_j) = \frac{2 \cdot \left|A_i \cap B_j\right|}{|A_i| + \left|B_j\right|}, i \in [1, n], j \in [1, m] \tag{13}$$

where $\|$ represents the width of the region (unit: pixel), $\mathrm{DSC}(A_i, B_j) \in [0, 1]$.

Let TP denotes true positive (TP). The values of TP in this paper can be calculated as follows:

$$\mathrm{TP} = \sum_{i=1}^{n} \sum_{j=1}^{m} (\mathrm{DSC}(A_i, B_j) > T) \tag{14}$$

where $i \in [1, n]$, $j \in [1, m]$. The expression $\mathrm{DSC}(A_i, B_j) > T$ is a logical expression. When its value is true, it is represented by the number 1. When its value is false, it is represented by the number 0. T is a threshold. If $\mathrm{DSC}(A_i, B_j) > T$, then we believe that B_i is a vulnerable plaque region. $T = 0.5$ is empirically recommended for medical images to optimize the trade-off between specificity and sensitivity according to our test and previous studies.[1]

Similarly, the values of false positive (FP) and false negative (FN) in this paper can be defined as follows:

$$\mathrm{FP} = \sum_{i=1}^{n}\sum_{j=1}^{m}((\mathrm{DSC}(A_i, B_j) > 0) \wedge (\mathrm{DSC}(A_i, B_j) \le T)) + \sum_{j=1}^{m}\left(\left(\sum_{i=1}^{n}(\mathrm{DSC}(A_i, B_j) = 0)\right) = 0\right) \quad (15)$$

$$\mathrm{FN} = \sum_{i=1}^{n}\left(\left(\sum_{j=1}^{m}(\mathrm{DSC}(A_i, B_j) = 0)\right) = 0\right) \quad (16)$$

Equation (15) indicates that if A_i and B_i are not similar ($0 < \mathrm{DSC}(A_i, B_j) \le T$), or there are no elements in set A that intersect with B_i, then we believe that B_j is not a vulnerable plaque region. Equation (16) indicates that if there is no element in set B that intersects with A_i, then the vulnerable plaque region A_i is missed by the system.

The value of true negative (TN) represents the number of samples that the doctor marked as negative and the system also detected as negative.

According to Eqs. (14)–(16), we can define the evaluation metrics for the detection of vulnerable plaques:

Precision rate:

$$P = \mathrm{TP}/(\mathrm{TP} + \mathrm{FP}) \quad (17)$$

where $P \in [0, 1]$.

Recall rate (Sensitivity):

$$R = \mathrm{TP}/(\mathrm{TP} + \mathrm{FN}) \quad (18)$$

where $R \in [0, 1]$.

Overlap rate:

$$\mathrm{D} = \frac{1}{\mathrm{TP}}\sum_{i=1}^{n}\sum_{j=1}^{m}\mathrm{DSC}(A_i, B_j), \quad \mathrm{DSC}(A_i, B_j) > T \quad (19)$$

where overlap rate D is the mean value of all DSC greater than T; $D \in [0, 1]$.

Detection quality score:

$$S = w_1 \times \frac{2P \times R}{P + R} + w_1 \times D, w_1, w_2 \in [0, 1], w_1 + w_2 = 1 \quad (20)$$

where $S \in [0, 1]$. The greater the S value, the better the result of detection. In this paper $w_1 = w_2 = 0.5$.

The metrics above were used in the challenge held by the second Chinese Conference on Computer Vision (CCCV 2017).

RESULTS

In this paper, 2000 training images and 300 test images provided by Shenzhen Vivolight Medical Device & Technology Co., Ltd were used for experiments.

Evaluation of Pre- and Post-processing Modules

We designed the ablation experiments shown in Table 2 to test the performance of pre- and post-processing modules. To simplify the experiment, only Faster R-CNN in the DCNN module in the system was enabled, and the ensemble module was disabled.

As can be seen from Table 2, we designed seven experiments to examine the performance of the pre- and post-processing methods. "Union of intersecting regions" was required in all experiments since the detected vulnerable plaques are not allowed to intersect with each other according to (12).

E1 was carried out directly without the pre- and post-processing. The results of E1 were taken as the baseline of the experiments below.

E2 was performed to evaluate the performance of "de-noising" for vulnerable plaque detection. Input images were processed by the de-noising

TABLE 2. Ablation experiments on the proposed system.

	No.						
Module/method	E1	E2	E3	E4	E5	E6	E7
Pre-processing							
De-noising		√		√		√	√
Data augmentation			√	√		√	√
Post-processing							
Union of Intersecting region	√	√	√	√	√	√	√
Duplicated region					√	√	√
Small gaps removal					√		√

The first column represents some of the modules in the system, and the second column represents the respective methods in the module. Methods in the module were combined to evaluate the impact of each method on the detection performance. The "√" in the table indicates that the method was used in the experiment listed in the same row.

method introduced in sections Pre-processing and De-noising. Then the processed data were input into the Faster R-CNN for detection.

E3 was performed to evaluate the performance of "data augmentation" for vulnerable plaque detection. Input images were processed using the data augmentation method introduce in sections Pre-processing and Data Augmentation. Then the processed data were input into the Faster R-CNN for detection.

E4 was designed to assess the performance of the pre-processing for vulnerable plaque detection.

E5 was designed to assess the performance of the post-processing for vulnerable plaque detection.

E6 was designed to assess the performance of all the methods in pre- and post-processing except the "small gaps removal" described in sections Post-processing and Small Gaps Removal.

E7 was carried out with both pre- and post-processing.

Table 3 lists the detection results of the experiments above.

We also analyzed the performance of pre- and post-processing for vulnerable plaque detection using SPSS software, and the ROC Curves were plotted in Fig. 6.

Figure 6 also shows the *area under curve* (AUC). We can see the maximum AUC is the AUC of E7 (0.867). This indicates that the detection performance achieves the best when the system enables both pre- and post-processing functions. These results were consistent with the results indicated by detection quality score.

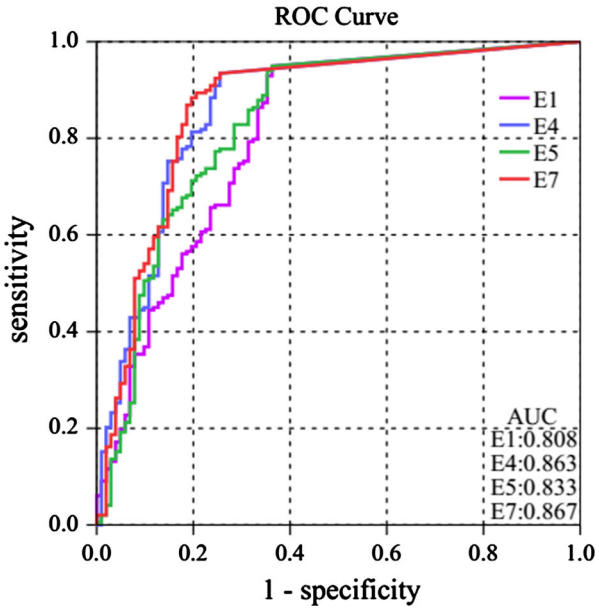

FIGURE 6. ROC curves and AUC for experiment E1, E4, E5, and E7. Note that pre- and post-processing were not applied to E1; pre-processing was applied to E4; E5 was carried out with post-processing while exclude pre-processing; both pre- and post-processing were applied to E7.

Evaluation of DCNN Module

We also conducted experiments with different networks in DCNN module to investigate its effect on the detection performance of vulnerable plaques. These networks include YOLO, SSD, and Faster R-CNN. For each experiment, only one single network was enabled, with the pre- and post-processing modules enabled, and the ensemble module disabled during the experiments. In addition, the results with traditional machine-learning algorithm Haar-Adaboost are also listed for comparison. Experimental results on the test set were recorded in the first 4 lines in Table 4.

Evaluation of Ensemble Module

We combined different networks (YOLO, SSD, and Faster R-CNN) in the DCNN module for ensembling experiments. The results output by different networks were combined using the vulnerable plaque region mergence rule described in the "ensemble" section. The detection results of the proposed system with various combinations of networks for ensembling are recorded in the last 4 lines in Table 4.

DISCUSSION

Comparison of Algorithm Results

Table 3 presents the evaluation results of the corresponding methods in the pre- and post-processing modules. The results of experiment E1 were obtained from the Faster R-CNN in the DCNN module. Its detection quality score is the lowest of all the results. It serves as the baseline for the following comparisons.

E2 verified the effect of de-noising in the pre-processing module on the detection performance of vulnerable plaque. Because the dark lumen region did not contain any information related to vulnerable plaque, we removed the noise in dark lumen region by the proposed de-noising method. From Table 3 we can see that the precision rate of E2 increased by 14 percentage points (pp) and the overlap rate of E2 increased by 8 pp compared with those of E1, but the recall rate was slightly reduced. The detection quality score was improved by about 8 pp.

The performance of data augmentation method was verified in E3. Data augmentation method, such as shifting, rotation, jittering, and random scale, has been widely used in deep learning.[23] How to choose a data augmentation strategy depends on the characteristics

TABLE 3. Detection results on the proposed test set.

Metrics No.	Precision rate (%)	Recall rate (%)	Overlap rate (%)	Detection quality score (%)
E1	55.20	95.50	73.79	71.88
E2	69.08	91.98	81.78	80.34
E3	70.80	93.16	78.53	79.49
E4	72.37	94.42	83.33	82.63
E5	67.42	95.24	80.79	79.87
E6	71.21	96.41	83.84	82.88
E7	78.75	96.43	84.03	85.36

TABLE 4. Detection results on the test set with different networks/Haar-Adaboost and with different combinations of networks.

	Metrics			
Network/method	Precision rate (%)	Recall rate (%)	Overlap rate (%)	Detection quality score (%)
Haar-Adaboost	40.41	57.56	68.00	57.74
YOLO	60.00	83.58	74.94	72.40
SSD	82.78	74.13	78.19	78.20
Faster R-CNN	78.75	96.43	84.03	85.36
YOLO + SSD	26.67	51.70	67.04	51.12
YOLO + Faster R-CNN	38.02	64.10	69.19	58.46
YOLO + SSD + Faster R-CNN	76.65	98.50	84.84	85.53
Proposed	88.84	95.02	85.09	88.46

Both pre- and post-processing modules were enabled during the experiments.

of the data set. In this paper, we used the end-to-end connection method to keep the topological relationship among regions (or between regions and image borders) unchanged. The results in Table 3 show that the precision rate of E3 increased by more than 15 pp and the overlap rate of E3 increased by about 5 pp. As a result, the detection quality score was improved 8 pp. This indicates that our proposed data augmentation strategy is suitable for this data set.

The pre-processing module was enabled in E4. As shown in Table 3, the results of E4 are better than the results of E2 and E3. This indicates that both denoising and data augmentation play an important role in detection.

We turned off the pre-processing module and enabled the post-processing module in E5. Compared with the results of E1, the precision rate and overlap rate of E5 were increased, but the increase was less than that of E4.

We enabled the pre-processing module and added "duplicated region processing" in the post-processing module in E6. The performance of vulnerable plaque detection increased obviously compared with the performance in E1.

Finally, we enabled both pre- and post-processing modules in E7. The results show that the precision rate, recall rate, and overlap rate increased compared with all experiments, and the detection quality score increased to 85.36%. From Table 3 we can see obviously that the proposed algorithm used in E7 overwhelmed the algorithms without pre- and post-processing at least 13% regarding the detection quality score. This shows that pre- and post-processing play a significant role in improving the detection performance of vulnerable plaque.

Table 4 shows the evaluation results of DCNN and ensemble module. From the first 4 lines in this table, we can see that the recall rate and the overlap rate of Faster R-CNN were far higher than that of other single networks or algorithms, while the precision rate was slightly lower than that of SSD. In general, the detect quality score of Faster R-CNN was the highest in comparison with other networks/algorithm. We can see that our proposed ensemble method improves the overall vulnerable plaque detection performance from the last 4 lines, and the detection quality score of our system can reach the highest value (88.46%).

Comparison of Previous Studies

In this section, we compared our method with the methods of previous studies.[6,10,22] The test set used for comparison were the same, and the evaluation metrics were the same.

Please note that both our method and the method in Refs. 6 and 22 are object detection methods which can localize plaque regions in an IVOCT image. We compared their performances in Table 5.

From Table 5 we can see that the method in Ref. 6 got the lowest values of performance metrics of all three methods when we applied it to our test set. This is mainly because the method in Ref. 6 uses traditional algorithms, such as *gray-level co-occurrence matrices* (GLCM) and *Fuzzy C-Means* (FCM) *clustering*, to detect plaques. The performance of these traditional algorithms are limited since the key parameters they used are non-adaptive for feature extraction and classification. Our method overwhelmed the method in Ref. 6 at least 46% regarding the detection quality score.

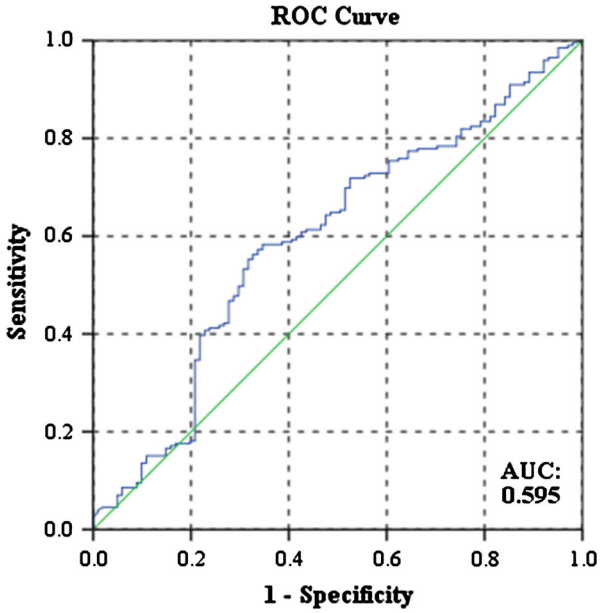

FIGURE 7. ROC curve and AUC for Jun's method.

The method in Ref. 22 is also a deep-learning-based method. Compared to this method, our method increased the detection quality score nearly 1 pp, which indicates our method achieves better performance.

We also investigated the previous methods which focus on vulnerable plaque classification. The main task of these methods is to determine whether there are vulnerable plaques in an IVOCT image,[10] not to localize the plaque region in an IVOCT image. Recent research by Jun et al. shows that their optimized CNN classifier performed best in vulnerable plaque classification in comparison with other traditional classifiers.[10] We compared the performance of our method with Jun's method in terms of vulnerable plaque classification. Table 6 lists the classification performance of Jun's method and our method. From Table 6 we can see that our method outperforms Jun's method: the precision rate increased by 12 pp, the recall rate increased by 28 pp, and the specificity increased by 28 pp. As Jun's CNN classifier was optimized for the case when both IVUS and IVOCT images were available, the performance of their method may be limited when it was applied to our test set that only IVOCT images were provided.

We also plotted the ROC Curve in Fig. 7 for Jun's method. The AUC was 0.595, which is lower than our method even only the Faster R-CNN in the DCNN module was enabled (0.867, see also Fig. 6).

TABLE 5. Performance comparison of the method in Refs. 6 and 22, and the proposed method.

	Metrics			
Network/method	Precision rate (*P*) (%)	Recall rate (*R*) (%)	Overlap rate (*D*) (%)	Detection quality score (*S*) (%)
Method in Ref. 6	13.15	23.24	67.22	42.01
Method in Ref. 22	80.77	94.50	88.24	87.67
Proposed	88.84	95.02	85.09	88.46

TABLE 6. Classification performance of Jun's method and the proposed method.

	Metrics			
Method	Precision rate (*P*) (%)	Recall rate (*R*) (%)	Specificity (%)	AUC
Jun's method	77.08	67.33	55.78	0.595
Proposed	88.84	95.02	84.15	0.867

The metric specificity was calculated according to the formulas in Ref. 10.

CONCLUSIONS

This paper presents an automatic detection system of vulnerable plaque for IVOCT image. Multiple DCNNs are combined to form an ensemble to detect vulnerable plaques in IVOCT images. In order to improve the detection performance of networks, the IVOCT images input into the networks are pre-processed by using the methods of de-noising and data augmentation. Then the pre-processed results are input into the DCNN module. The output results of each network in DCNN module are post-processed by means of the union of intersecting regions, duplicated region processing, and small gaps removal. Finally, the output detection results of multiple networks are combined to form results. The detection quality score of our system achieved 88.46%. Our system can be used as an auxiliary diagnostic tool for vulnerable plaque detection in IVOCT images.

FUNDING

This study was funded by the Fundamental Research Funds for the Central Universities (2018CDXYJSJ0026), the Chongqing Foundation & Advanced Research Project (cstc2019jcyj-msxmX0622), the Science and Technology Research Program of Chongqing Municipal Education Commission (KJQN201800111), Sichuan Science and Technology Program (2019YFSY0026), and the Entrepreneurship and Innovation Program for Chongqing Overseas Returned Scholars (cx2017094).

CONFLICT OF INTEREST

Ran Liu, Yanzhen Zhang, Yangting Zheng, Yaqiong Liu, Yang Zhao, and Lin Yi declare that they have no conflicts of interest.

ETHICAL APPROVAL

All procedures performed in studies involving human participants were in accordance with the ethical standards of the institutional and/or national research committee and with the 1964 Helsinki declaration and its later amendments or comparable ethical standards. Informed consent was obtained from all individual participants included in the study. This article does not contain any studies with animals performed by any of the authors.

REFERENCES

[1]Baum, K. G., E. Schreyer, S. Totterman, J. Farber, J. Tamez-Peña, and P. González. Application of the Dice Similarity Coefficient (DSC) for Failure Detection of a Fully-Automated Atlas Based Knee MRI Segmentation Method. ISMRM Annual Meeting. 1–7 May 2010; Stockholm, Sweden 2010. p. 88.

[2]Campbell, I. C., D. P. Giddens, R. Virmani, A. Veneziani, S. T. Rab, H. Samady, *et al*. Computational fluid dynamics simulations of hemodynamics in plaque erosion. *Cardiovasc. Eng. Technol*. 4(4):464–473, 2013.

[3]Cao, Y., H. Lee, and H. Kwon. Enhanced Object Detection via Fusion With Prior Beliefs from Image Classification. 2017 IEEE International Conference on Image Processing. 17–20 Sept. 2017. IEEE, Beijing, China, 2017.

[4]Cho, K. Y., H. Miyoshi, S. Kuroda, H. Yasuda, K. Kamiyama, J. Nakagawara, *et al*. The phenotype of infiltrating macrophages influences arteriosclerotic plaque vulnerability in the carotid artery. *J. Stroke Cerebrovasc. Dis*. 22(7):910–918, 2013. https://doi.org/10.1016/j.jstrokecerebrovasdis.2012.11.020.

[5]Costopoulos, C., A. J. Brown, Z. Teng, S. P. Hoole, N. E. J. West, H. Samady, *et al*. Intravascular ultrasound and optical coherence tomography imaging of coronary atherosclerosis. *Int. J. Cardiovasc. Imaging* 32(1):189–200, 2016. https://doi.org/10.1007/s10554-015-0701-3.

[6]Dehnavi, S. M., M. S. P. Babu, M. Yazchi, and M. Basij. Automatic soft and hard plaque detection in IVUS images: a textural approach. 2013 IEEE Conference on Information & Communication Technologies; 11–12 April 2013. IEEE, Thuckalay, Tamil Nadu, India, 2013. pp. 214–219.

[7]Devarakonda, S. T., K. K. Vupparaboina, A. Richhariya, J. Chhablani, and S. Jana. Automated detection of retinal disorders from OCT images using artificial neural network. 2016 IEEE Annual India Conference, 16–18 Dec. 2016. IEEE, Bangalore, India, 2017, pp. 1–6.

[8]Hou, W., and L. Wang. Application of mathematical morphology and canny operator in pattern extraction of wood decay image. International Conference on Computer Science and Network Technology. 24–26 December 2011. IEEE, Harbin, China, 2011, pp. 306–309.

[9]Huang, Z., W. Dong, H. Duan, and J. Liu. A regularized deep learning approach for clinical risk prediction of acute coronary syndrome using electronic health records. *IEEE Trans. Biomed. Eng*. 65(5):956–968, 2018. https://doi.org/10.1109/TBME.2017.2731158.

[10]Jun, T. J., S.-J. Kang, J.-G. Lee, J. Kweon, W. Na, D. Kang, *et al*. Automated detection of vulnerable plaque in intravascular ultrasound images. *Med. Biol. Eng. Comput*. 57(4):863–876, 2019. https://doi.org/10.1007/s11517-018-1925-x.

[11]Kubo, T., T. Imanishi, M. Kashiwagi, H. Ikejima, H. Tsujioka, A. Kuroi, *et al*. Multiple coronary lesion instability in patients with acute myocardial infarction as determined by optical coherence tomography. *Am. J. Cardiol*. 105(3):318–322, 2010. https://doi.org/10.1016/j.amjcard.2009.09.032.

[12]Kubo, T., Y. Ino, T. Tanimoto, H. Kitabata, A. Tanaka, and T. Akasaka. Optical coherence tomography imaging in acute coronary syndromes. *Cardiol. Res. Pract*. 2011(1):312978, 2011. https://doi.org/10.4061/2011/312978.

[13]Kume, T., H. Okura, R. Yamada, T. Kawamoto, N. Watanabe, Y. Neishi, *et al*. Frequency and spatial distribution of thin-cap fibroatheroma assessed by 3-vessel intravascular ultrasound and optical coherence tomography: an ex vivo validation and an initial in vivo feasibility study. *Circ. J.* 73(6):1086–1091, 2009. https://doi.org/10.1253/circj.cj-08-0733.

[14]Li, X., J. Li, J. Jing, T. Ma, S. Liang, J. Zhang, *et al*. Integrated IVUS-OCT imaging for atherosclerotic plaque characterization. *IEEE J. Sel. Top. Quantum Electron.* 20(2):7100108, 2014. https://doi.org/10.1109/JSTQE.2013.2274724.

[15]Li, H., X. Wang, and S. Ding. Research and development of neural network ensembles: a survey. *Artif. Intell. Rev.* 2:1–25, 2017. https://doi.org/10.1007/s10462-016-9535-1.

[16]Liu, W., D. Anguelov, D. Erhan, C. Szegedy, S. Reed, C. Y. Fu, *et al*. Single Shot MultiBox Detector. In: 14th European Conference on Computer Vision. October 11–14 2016. Springer, 2016, pp. 21–37.

[17]López-Tapia, S., R. Molina, and N. P. D. L. Blanca. Deep CNNs for object detection using passive millimeter sensors. In: IEEE Transactions on Circuits & Systems for Video Technology. 2017, vol. 99, pp. 1–. https://doi.org/10.1109/TCSVT.2017.2774927.

[18]Redmon, J., S. Divvala, R. Girshick, and A. Farhadi. You Only Look Once: Unified, Real-Time Object Detection. In: 29th IEEE Conference on Computer Vision and Pattern Recognition. 27–30 June 2016. IEEE, Las Vegas, NV, USA, 2016, pp. 779–788.

[19]Rembold, D., R. Kromer, L. Wagenfeld, and R.-R. Grigat. An automated approach for inner segment/outer segment defect detection in retinal SD-OCT images. *J. Med. Biol. Eng.* 38(4):646–653, 2018. https://doi.org/10.1007/s40846-018-0377-y.

[20]Ren, S., R. Girshick, R. Girshick, and J. Sun. Faster R-CNN: towards real-time object detection with region proposal networks. *IEEE Trans. Pattern Anal. Mach. Intell.* 39(6):1137–1149, 2017. https://doi.org/10.1109/TPAMI.2016.2577031.

[21]Shah, P. K. Role of inflammation and metalloproteinases in plaque disruption and thrombosis. *Vasc. Med.* 3(3):199–206, 1998. https://doi.org/10.1191/135886398676959944.

[22]Shi, P., J. Xin, S. Liu, Y. Deng, and N. Zheng. Vulnerable plaque recognition based on attention model with deep convolutional neural network. In: Annual International Conference of the IEEE Engineering in Medicine and Biology Society. IEEE Engineering in Medicine and Biology Society, Honolulu, HI, USA. IEEE, 18–21 July 2018, pp. 834–837.

[23]Shijie, J., W. Ping, J. Peiyi, and H. Siping, editors. Research on data augmentation for image classification based on convolution neural networks. 2017 Chinese Automation Congress. 20–22 October 2017. IEEE, Jinan, China, 2017.

[24]Takai, H., J. Uemura, Y. Yagita, Y. Ogawa, K. Kinoshita, S. Hirai, *et al*. Plaque characteristics of patients with symptomatic mild carotid artery stenosis. *J. Stroke Cerebrovasc. Dis.* 27(7):1930–1936, 2018. https://doi.org/10.1016/j.jstrokecerebrovasdis.2018.02.032.

[25]Viola, P., and M. Jones. Rapid object detection using a boosted cascade of simple features. In: 2001 IEEE Computer Society Conference on Computer Vision and Pattern Recognition. IEEE, Kauai, HI, USA, 2001, pp. I-511-I-8.

[26]Wang, Z., D. Chamie, H. G. Bezerra, H. Yamamoto, J. Kanovsky, D. L. Wilson, *et al*. Volumetric quantification of fibrous caps using intravascular optical coherence tomography. *Biomed. Opt. Express* 3(6):1413–1426, 2012. https://doi.org/10.1364/BOE.3.001413.

[27]Wang, Z., H. Jia, J. Tian, T. Soeda, R. Vergallo, Y. Minami, *et al*. Computer-aided image analysis algorithm to enhance in vivo diagnosis of plaque erosion by intravascular optical coherence tomography. *Circ. Cardiovasc. Imaging* 7(5):805–810, 2014. https://doi.org/10.1161/CIRCIMAGING.114.002084.

[28]Wang, A., and X. Tang, editors. Automatic segmentation of vessel lumen in intravascular optical coherence tomography images. In: IEEE International Conference on Mechatronics and Automation. 7–10 August 2016. IEEE, Harbin, China, 2016.

[29]Xu, M., J. Cheng, D. W. Wong, A. Taruya, A. Tanaka, and J. Liu. Automatic atherosclerotic heart disease detection in intracoronary optical coherence tomography images. In: 36th Annual International Conference of the IEEE Engineering in Medicine and Biology Society, 26–30 August 2014. IEEE, Chicago, IL, USA, 2014, pp. 174–177.

[30]Xu, M., J. Cheng, D. W. K. Wong, A. Taruya, A. Tanaka, J. Liu, *et al*, editors. Automatic image classification in intravascular optical coherence tomography images. In: 2016 IEEE Region 10 Conference, 2016 22–25 November 2016. IEEE, Singapore, Singapore.